Aftershock seismicity of the 27 February 2010 *Mw* 8.8 Maule earthquake rupture zone

Dietrich Lange [a,b,*], Frederik Tilmann [b,c], Sergio E. Barrientos [d], Eduardo Contreras-Reyes [d], Pascal Methe [e,b], Marcos Moreno [b], Ben Heit [b], Hans Agurto [f], Pascal Bernard [g], Jean-Pierre Vilotte [g], Susan Beck [h]

[a] University of Potsdam, Germany
[b] GFZ German Research Center for Geosciences, Potsdam, Germany
[c] Institut für Geologische Wissenschaften, Freie Universität Berlin, Germany
[d] Departamento de Geofísica, Facultad de Ciencias Físicas y Matemáticas, Universidad de Chile, Santiago, Chile
[e] University of Jena, Germany
[f] University of Liverpool, UK
[g] Institut de Physique du Globe de Paris, France
[h] University of Arizona, Tucson, USA

ARTICLE INFO

ABSTRACT

On 27 February 2010 the M_w 8.8 Maule earthquake in Central Chile ruptured a seismic gap where significant strain had accumulated since 1835. Shortly after the mainshock a dense network of temporary seismic stations was installed along the whole rupture zone in order to capture the aftershock activity. Here, we present the aftershock distribution and first motion polarity focal mechanisms based on automatic detection algorithms and picking engines. By processing the seismic data between 15 March and 30 September 2010 from stations from IRIS, IPGP, GFZ and University of Liverpool we determined 20,205 hypocentres with magnitudes M_w between 1 and 5.5. Seismic activity occurs in six groups: 1.) Normal faulting outer rise events 2.) A shallow group of plate interface seismicity apparent at 25–35 km depth and 50–120 km distance to the trench with some variations between profiles. Along strike, the aftershocks occur largely within the zone of coseismic slip but extend ~50 km further north, and with predominantly shallowly dipping thrust mechanisms. Along dip, the events are either within the zone of coseismic slip, or downdip from it, depending on the coseismic slip model used. 3.) A third band of seismicity is observed further downdip at 40–50 km depth and further inland at 150–160 km trench perpendicular distance, with mostly shallow dipping (~28°) thrust focal mechanisms indicating rupture of the plate interface significantly downdip of the coseismic rupture, and presumably above the intersection of the continental Moho with the plate interface. 4.) A deep group of intermediate depth events between 80 and 120 km depth is present north of 36°S. Within the Maule segment, a large portion of events during the inter-seismic phase originated from this depth range. 5.) The magmatic arc exhibits a small amount of crustal seismicity but does not appear to show significantly enhanced activity after the M_w 8.8 Maule 2010 earthquake. 6.) Pronounced crustal aftershock activity with mainly normal faulting mechanisms is found in the region of Pichilemu (~34.5°S). These crustal events occur in a ~30 km wide region with sharp inclined boundaries and oriented oblique to the trench. The best-located events describe a plane dipping to the southwest, consistent with one of the focal planes of the large normal-faulting aftershock ($M_w = 6.9$) on 11 March 2010.

1. Introduction

The majority of global earthquakes occur along subduction zones. During great earthquakes ($M \geq 8$) the shallowly dipping interface between the plates ruptures down to depths of up to 50 km (Oleskevich et al., 1999), while the rupture propagates along the margin. The properties of the plate interface are heterogeneous which is reflected by the complex pattern of kinematic coupling between the plates (Chlieh et al., 2008) and spatially variable coseismic slip distributions (Konca et al., 2008; Moreno et al., 2009). The distribution of aftershock activity also shows complex distributions that may correlate with zones of high post-seismic strain (Das and Henry, 2003). Often, the aftershocks cluster around the coseismic rupture area due to elevated differential stresses (Mendoza and Hartzell, 1988). Here, we study the aftershock series of the 27 February 2010 M_w 8.8 Maule earthquake in Central Chile which offers the possibility to study the heterogeneous structure and processes of subduction zones due to the large amount of aftershock activity associated with this subduction zone event.

* Corresponding author at: University of Potsdam, Germany.
  E-mail address: dietrich.lange@uni-potsdam.de (D. Lange).

2. Tectonic setting and the 27 February 2010 the M_w 8.8 Maule earthquake

The M_w 8.8 Maule earthquake on 27 February 2010 is the sixth largest earthquake since the beginning of instrumental seismology. Before the 2010 earthquake, GPS measurements showed the plate interface to be strongly coupled (Ruegg et al., 2009) and other megathrust earthquakes, notably the 1928 $M_s = 8.0$ (Beck et al., 1998) in the region of the 2010 Maule earthquake released only a small fraction of the strain accumulated due to the plate convergence. The Maule earthquake thus filled a seismic gap (Campos et al., 2002; Comte et al., 1986; McCann et al., 1979) that has experienced little seismic activity since 1835, when it broke completely (Darwin, 1840). However, the Maule 2010 earthquake might not have released all the stress and there might still be the potential for a large event (Lorito et al., 2011; Moreno et al., 2011).

The Maule 2010 rupture initiated at ~36.5°S, and ruptured bilaterally with two major slip patches (Delouis et al., 2010; Lay et al., 2010; Lorito et al., 2011; Pollitz et al., 2011; Tong et al., 2010). The stronger northern patch is characterised by a peak slip of 15–20 m and coincides approximately with the most probably 1928 rupture zone (Fig. 1), and abuts to the north against the rupture area of the 1985 event ($M_w = 7.9$), with aftershocks reaching further north well into the 1985 area. The northern end of the rupture is located near the subducted Juan Fernández Ridge (~32.5°S) which is a major tectonic boundary (Yáñez et al., 2001) but the Maule 2010 earthquake stops 80 km (aftershocks)–150 km (main rupture patch) south of the intersection of the subducted ridge with the Chilean Forearc (Figs. 1 and 2). The southern patch of the 2010 Maule event with a peak slip of ~10 m (Lorito et al., 2011; Pollitz et al., 2011; Tong et al., 2010) overlaps with the epicentral region of the M_w 9.5 1960 earthquake (Moreno et al., 2009; Plafker and Savage, 1970) around 110 km. The southern termination of the 2010 Maule event coincides reasonably well with the major asperity of the 1960 earthquake sequence (Lorito et al., 2011) which had more than 30 m of slip (Fig. 1).

3. Earthquake data

In response to the M_w 8.8 Maule earthquake on 27 February 2010 Chilean and international seismologists installed a dense seismological network (International Maule Aftershock Deployment, IMAD), which covers the whole length of the rupture zone between 32.5°S and 38.5°S (Fig. S1). We have determined automated hypocentres for local seismicity using 58 stations from IRIS (http://www.iris.edu/hq/chile/), 41 stations from IPGP and Caltech (https://www.lia-mb.net/), 30 stations from GFZ (http://geofon.gfz-potsdam.de/geofon/) and 17 stations from the University of Liverpool. Most stations were deployed within 1 month after the mainshock and the best station coverage was achieved between April 1 and June 1, 2010 with more than 130 running stations. The station spacing is ~30 km and allows a good resolution of hypocentral coordinates, including depth. Due to the rainy season starting in June to July and changes in the station configuration the network coverage varies spatially and temporally (Fig. S2); on average, 75 stations were operational between July and 30 September 2010.

4. Data processing

4.1. Event detection and automated phase picking

In a first step, events were detected with Coalescence Microseismic Mapping (CMM, Drew et al., 2005), an algorithm based on backpropagating STA/LTA based arrival pick probability density functions. The application of CMM using continuous waveform data from up to 80 selected stations between 15 March and 30 September 2010 resulted in the detection of 85,067 potential events with SNR > 2.5.
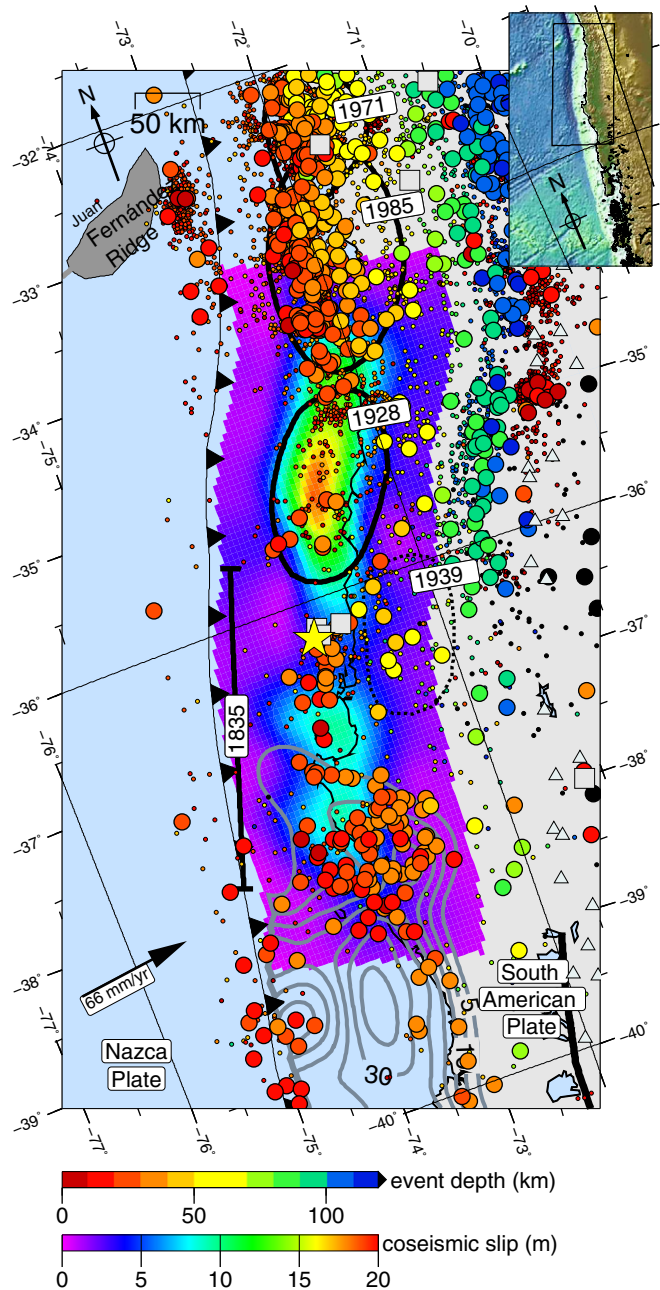
Fig. 1. Location map showing the oblique subduction and historical earthquakes along the Chilean margin (inset: overview map showing GTOPO2 topography/bathymetry). The seismicity before the M_w 8.8 Maule earthquake of 27 February 2010 (yellow star: main shock epicentre in SSN catalogue) from the EHB catalogue (1960–2009) and the SSN catalogue (2001–26/02/2010) is shown with large and small circles, respectively. Grey squares indicate earthquakes before the 2010 rupture between 01 January 2010 and 26 February 2010 (NEIC catalogue). The coseismic slip distribution of the 2010 Maule event from Lorito et al. (2011) is shown with colour, and the slip distribution of the 1960 earthquake based on the inversion of land-level changes Moreno et al. (2009) is shown with grey lines (5 m slip contours). Arrow shows plate convergence after Angermann et al. (1999). Holocene volcanoes are shown as triangles. The intermediate depth event of 1939 is shown with a dashed line (Beck et al., 1998). Rupture zones of other previous large and great earthquakes shown with black lines: 1835 and 1928 events from Campos et al. (2002); 1971 earthquake from Barrientos (1995); 1985 event from Barrientos (1988). The crustal, dextral Liquiñe–Ofqui fault zone which is located parallel to the magmatic arc south of 39°S is shown with a black line (Lange et al., 2008).

In a second step the automated hypocentral estimates were used to calculate P arrival times for the individual stations using the minimum 1D velocity model from Haberland et al. (2009). Last,
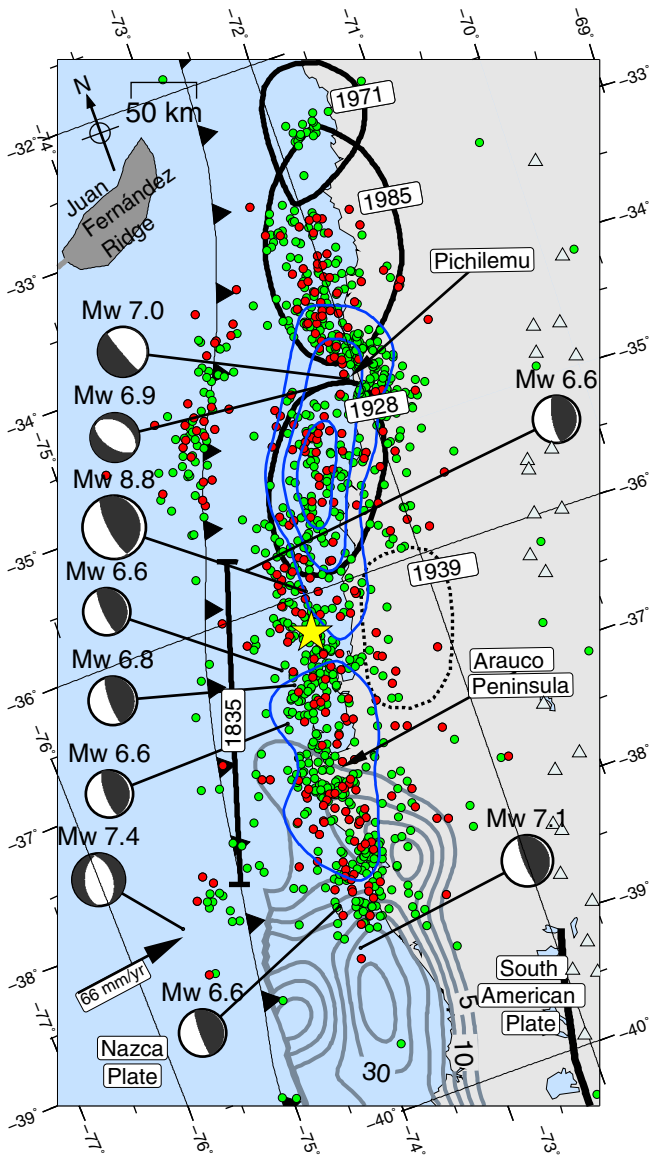
Fig. 2. Map showing the aftershock seismicity from the NEIC catalogue (27/02/2010 until 16/06/2011, $M \geq 4.5$). Events during the first 24 h after the mainshock are shown in red. Centroid locations and double-couple components from moment tensors of large aftershocks of the 2010 Maule earthquake (Global CMT catalogue, $M_w \geq 6.5$, lower hemisphere projection, 27/02/2010 until 26/02/2011) are shown in black. Coseismic slip distribution of the 2010 Maule event from Lorito et al. (2011) is shown with blue lines (5 m slip contours). Other lines and symbols are the same as in Fig. 1.

weights were comparable to a human analyst (Di Stefano et al., 2006), but the "hit-rate" of MPX was less than the rate from an human analyst because of the (conservative) tendency of the algorithm to downgrade a number of high quality picks. For the Maule dataset 182 events were picked manually as a reference dataset. We assigned each manually picked arrival a quality label (weight) according to the uncertainty (0: 0.05 s; 1: 0.1 s; 2: 0.2 s; 3: 0.4 s). MPX only finds 75% of the arrivals compared to a human picker. After comparison of the automated picks with the manually picked reference dataset (Fig. 3A–D) we accepted MPX P-onsets with qualities 0, 1 and 2. The average differences between manual and automatic picks for these qualities were 0.03, 0.04 and 0.09 s, respectively. P-arrivals with a quality of 3 had a standard deviation of 0.15 s and were not used for this study. Even though most of these 1,143,079 arrivals indicate actual arrivals, many arrivals of this quality class include outliers due to noise and phase misidentification by MPX. After relocating the events with HYP (Lienert and Havskov, 1995) we removed 1507 (0.39%) arrivals where the ratio of station residual and distance is larger than 0.05 s/km in order to remove large outliers which are mostly due to traffic or animal noise and GPS timing problems. The distance-dependent threshold is chosen in order to allow arrivals from stations far away to have larger residuals. Lastly, we removed all events with less than 8 P-arrivals or RMS more than 1 s. In total, 354,379 P arrivals from 20,205 events remain, which should almost all represent tectonic events with well determined epicentres.
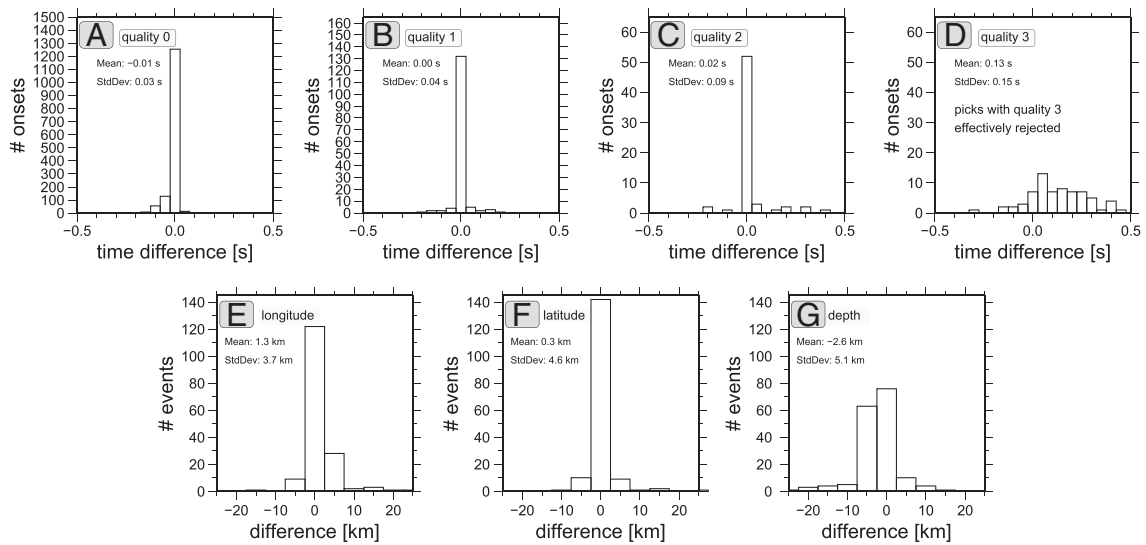
4.2. Inversion for 1D v_p velocity model

The velocity structure in the southern part of the Maule 2010 rupture is well constrained by Haberland et al. (2006, 2009) between 37° and 39°S. Therefore, we inverted for a minimum one-dimensional (1D) v_p velocity model for the northern part of the 2010 Maule rupture area and station statics using VELEST (Kissling et al., 1994). For the joint inversion we selected events inside the network (GAP ≤ 180°) from the northern part of the Maule 2010 rupture zone (33.5°–36°S) with at least 35 P arrivals per event, leading to 23,124 P-onsets from 530 events for the joint inversion. We generate 16,500 starting models (within the corridor marked by dashed lines in Fig. 4) and show the 50 models with the lowest RMS to gauge the depths at which the model is well resolved. The model is very tightly constrained between 10 and 50 km, and has some resolution at 5–10 and 50–70 km (Fig. 4A). It is very similar to the minimum 1D v_p model of Haberland et al. (2006), except that it has slightly slower velocities at 40–50 km depth, i.e., there appears to be only limited N/S variation of the structure. Station terms were re-determined for our 1D minimum v_p model using a subset of events from the whole rupture zone chosen to achieve an approximately even distribution of events in N/S direction and in depth (Fig. 4B). Then, all 20,205 events were relocated in our minimum 1D v_p velocity model with the single event mode from VELEST (Kissling et al., 1994) (Fig. S3). To validate the approach described above we detected and located independently the 2010 Maule aftershock series with the Binder code (Nippress et al., 2010), which is based on automatic phase association of potential arrivals determined from an STA/LTA picker; this resulted in a similar seismicity distribution (Fig. S4).

4.3. Final catalogue based on a priori quasi-2D velocity model and error estimates

Finally, we construct a quasi-2D model by taking the EW-oriented 2D-tomographic model of Haberland et al. (2009) and transposing it across the whole study region by following the geometry of the trench (i.e., for each latitude, the model is shifted in EW direction to keep distances to the trench of all model features constant). This approach is justified by the similarity of the 1D v_p velocity models

we applied the MPX picking algorithm (Aldersons, 2004) to 3.2×10^6 potential arrivals on vertical components in order to measure automatically P arrival times and determine onset polarities. For each of the stations within 200 km distance of the first epicentral estimate from CMM we applied a series of MPX runs on time windows starting 5 s before and stopping 5 s after the predicted arrival time with steps of 0.5 s. If multiple onsets were found by MPX during this time window we accepted the arrival with the highest quality. In case more than one arrival with the same quality was found by MPX we accepted the earliest onset. Although 6.4×10^7 MPX runs had to be calculated, this approach has the advantage that it results in picks of consistent quality with assigned weights where the arrivals with the highest quality (0,1) are potentially usable for tomography studies (Diehl et al., 2009). In a previous study, MPX arrival times and

Fig. 3. Top (A–D): Difference of v_p arrival times between automated and manual picks. 6629 automated MPX P-arrival times of 182 events were manually revised, both for their onset times and qualities. The histograms show the time difference of the picks which were assigned the same quality by the automated and manual picking. Negative times indicate arrivals where the automated picks are earlier in comparison to the manually determined onsets. Picks with quality class 3 were not used in this study. Bottom (E–G): Histograms showing the difference of the automated locations and manually picked events (based on P and S arrivals). E: Difference in longitude. F: Difference in latitude. G: Depth difference.

from the Pichilemu region and the Arauco Peninsula (Fig. 4A) indicating limited along-strike variation of v_p along the Maule 2010 rupture area.

For location we use the non-linear oct-tree search algorithm (Non-LinLoc, Lomax et al., 2000). Travel times in the model are calculated using the finite-difference solution to the Eikonal equation (Podvin and Lecomte, 1991) with a grid spacing of 2 km. The oct-tree algorithm provides more reliable information on location uncertainties than linearized inversions by exploring the probability density functions

(PDF) of each individual event. The maximum likelihood location is chosen as the preferred location (Fig. 5). For each event NonLinLoc estimates a 3D error ellipsoid (68% confidence) from the PDF scatter samples. Station statics account for localised deviations from the a priori model and are determined from the average residual at a station. The relocation in the Haberland et al. (2009) based model resulted in smaller RMS and station terms than the relocation in the minimum-1D model (Table S1 and Fig. 4) and an alternative 3D
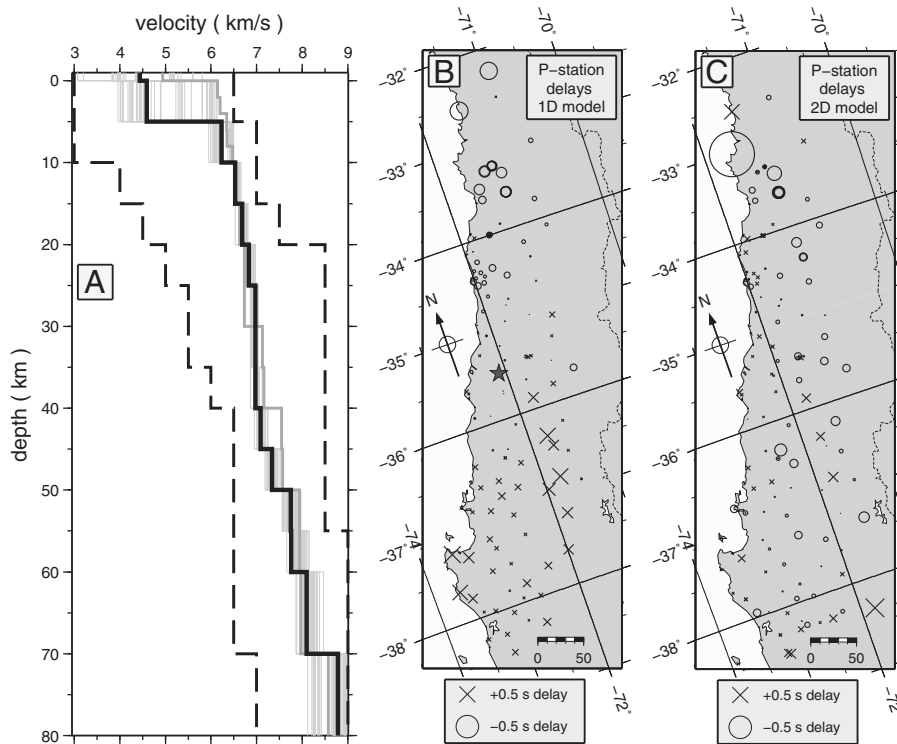
Fig. 4. (A) Minimum 1D v_p velocity model for the northern part of the 2010 Maule rupture area derived from local events between 33.5° and 36°S is shown with a black line. A linearised inversion for model and station statics using VELEST (Kissling et al., 1994) was calculated for 16,500 different starting models covering the v_p velocity space between the two dashed lines. The 50 models with the lowest RMS are shown by thin grey lines. Thick grey line shows minimum 1D v_p model of Haberland et al. (2009) for comparison. (B): Plot showing the station corrections for the minimum 1D model using 535 equally distributed events along the 2010 Maule rupture zone with 15,347 arrivals of highest quality (0 and 1). The reference station is marked with a star. (C): P-station corrections after three iterations with NonLinLoc using the 2D velocity model of Haberland et al. (2009).
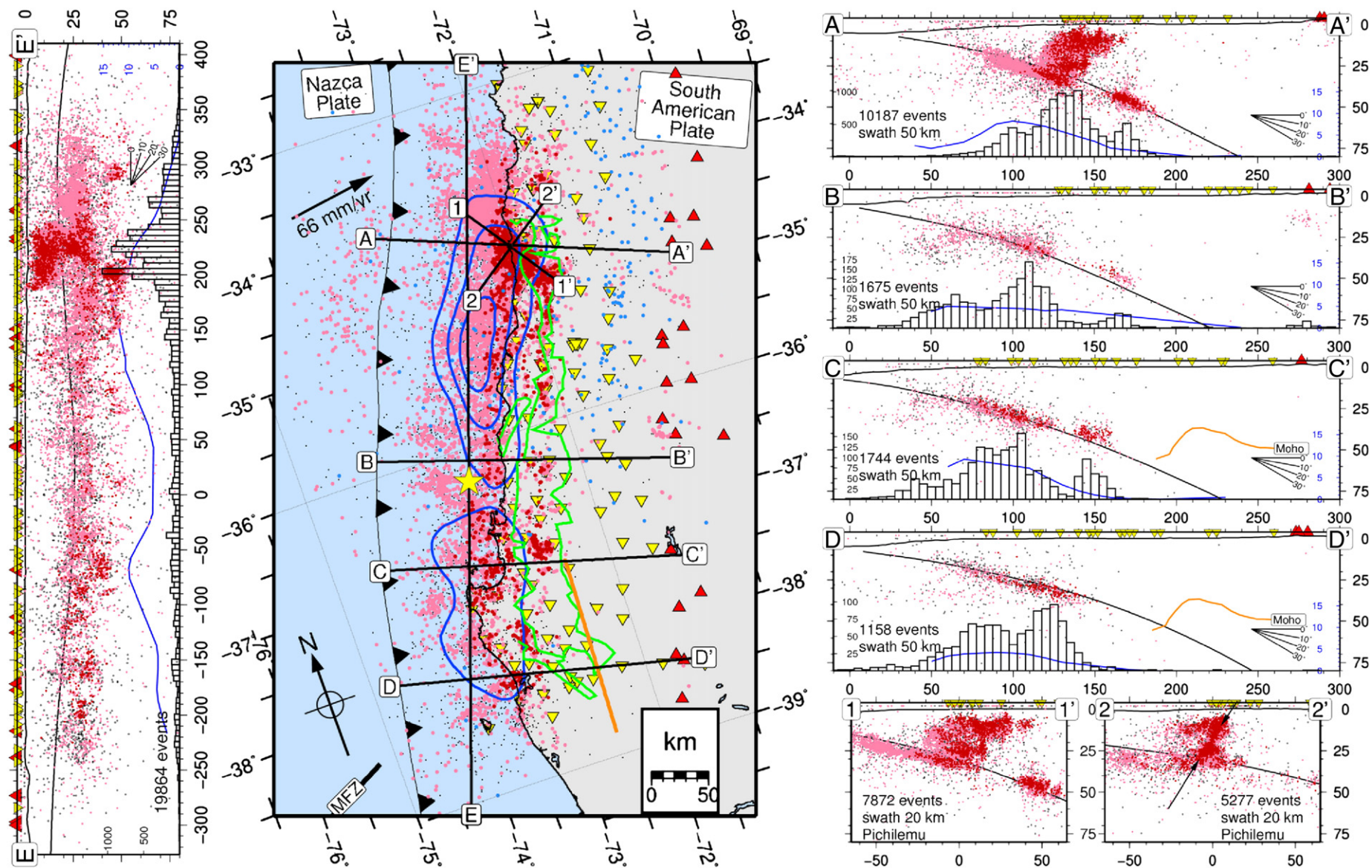
Fig. 5. Map and profiles showing the distribution of aftershocks between 15 March and 30 September 2010. 13,438 events with more than 12 P arrivals are shown with pink circles and further 6766 events with more than 8 P arrivals are shown with small black points. A high-quality subset of 2494 events (NonLinLoc parameters: maxlen3 = 5 km, minprob = 0.05, rmsmax = 0.6 s, nrdgsmin = 8, maxgap = 220°) is shown with red circles. Stations are shown with yellow inverted triangles, Holocene volcanoes as red triangles. Centre: Mapview with hypocentre locations and location of profiles. Events with depths greater than 80 km are shown with blue circles. The orange line indicates the location of intersection from continental mantle with the plate interface from local earthquake tomography (Haberland et al., 2009). Coseismic slip distribution of the 2010 Maule event Lorito et al. (2011) is shown with blue contourlines (5, 10 and 15 m contours). The green line indicates the location of the Late Paleozoic batholith (Martin et al., 1999). MFZ: Mocha Fracture Zone. Left and right panels: Vertical profiles showing the local seismicity together with the global slab model (Hayes and Wald, 2009); the location of the profiles is indicated in the map view. The histograms show the number of local aftershocks events along the sections together with the coseismic slip distribution in blue (Lorito et al., 2011). In panels C and D the orange line indicates the location from the continental Moho (inferred from the v_p 7.5 km/s contourline) from Haberland et al. (2009). Events are shown within 50 km (20 km) of either side for profiles A–E (1–2). Black arrows in profile 2–2′ indicate the southwest dipping seismicity cluster, consistent with the southwest dipping focal planes of the M_w 6.9 normal faulting event on 11 March 2010.

model constructed on the basis of global crust and slab models (CRUST2.0: Bassin et al., 2000; SLAB1.0: Hayes and Wald, 2009). In order to assess the quality of the final hypocentre locations we calculated regionalised mean lengths of the error ellipsoid for regions of $0.25 \times 0.25°$ tiles from the 3D error ellipsoids in latitude, longitude and depth direction (Fig. 6). The semi-axes of the mean error ellipsoid (68% confidence) are shorter than 5 km for most of the regions within the network for the individual directions. Events located off-shore or far away from the network become progressively less reliable with increasing distance from the coast and should be interpreted with caution.

Furthermore, we compared the hypocentres of the automated catalogue with the manually picked and revised events. 132 of these events are located within the network and include all events for which focal mechanisms could be estimated (see Section 4.5). The standard deviation for latitude and longitude is ~4 km and ~5 km for depths (Fig. 3E–G) for events within the network (GAP ≤ 180°) again indicating good resolution of events within the network.

4.4. Magnitudes

Moment magnitudes (M_w) were estimated using the automated procedure of Ottemöller and Havskov (2003), and local magnitudes (M_l) with the formula from Hutton and Boore (1987) using standard values for geometric spreading and attenuation. For the calculation of M_l and M_w ~800,000 automated amplitudes (spectra) were estimated. The resulting catalogue lists events with M_w between 0.9 and 5.5 (Fig. 7), with an approximate overall magnitude of completeness of approximately 3.5 (Fig. 7D). The magnitude of completeness varies spatially due to the differences in station coverage and temporally due to lower performance of the network during the rainy season starting in June to July (Fig. S2). For small M_l

($\leq$~3), the slope of the M_w to M_l curve is approximately 2/3, and for larger M_l the slope is approaching 1 (Fig. 7A), with a transition near M_l~4. This behaviour corresponds to theoretical expectations based on the definitions of M_w and M_l, where the rollover magnitude is determined by the maximum recordable frequency due to attenuation and instrumental limitations (Hanks and Boore, 1984). The relationship is in fact very similar to the one found for southern and central California, except that the rollover point is at M_l~2.5 in California (Hanks and Boore, 1984). For large events ($M_l > 5.5$), a large number of clipped traces results in uncertain magnitude estimates. The local M_w estimates are on average 0.5 (1) magnitude steps below the M_b (M_w) estimates of NEIC (Fig. S5) for events in both catalogues (Fig. 7C) but the local M_l estimates are comparable to the M_l estimates of the SSN catalogue (Fig. 7B).

4.5. Focal mechanisms

First motion polarities of P onsets for 110 stronger events were manually revised and focal mechanisms based on these first motion polarities were calculated following Reasenberg and Oppenheimer (1985). Take-off angles and azimuths were based on the 3D ray-tracing in the quasi-2D model described in Section 4.3. 77 events (with more than 15 P polarities) produced a unique solution. In order to compare the focal mechanisms estimated from the local network data and the Global CMT catalogue we calculated the bias in location as a weighted average for the 51 events that the Global CMT catalogue and the local aftershock catalogue have in common. The locations from the Global CMT catalogue are displaced 14 ± 9 km southwards and 7 ± 6 km westwards relative to the locally determined locations allowing a meaningful comparison between both. Fig. 8 shows the focal mechanisms from the local deployment together with the double-couple components of the Global CMT catalogue, plotted at their centroid locations.
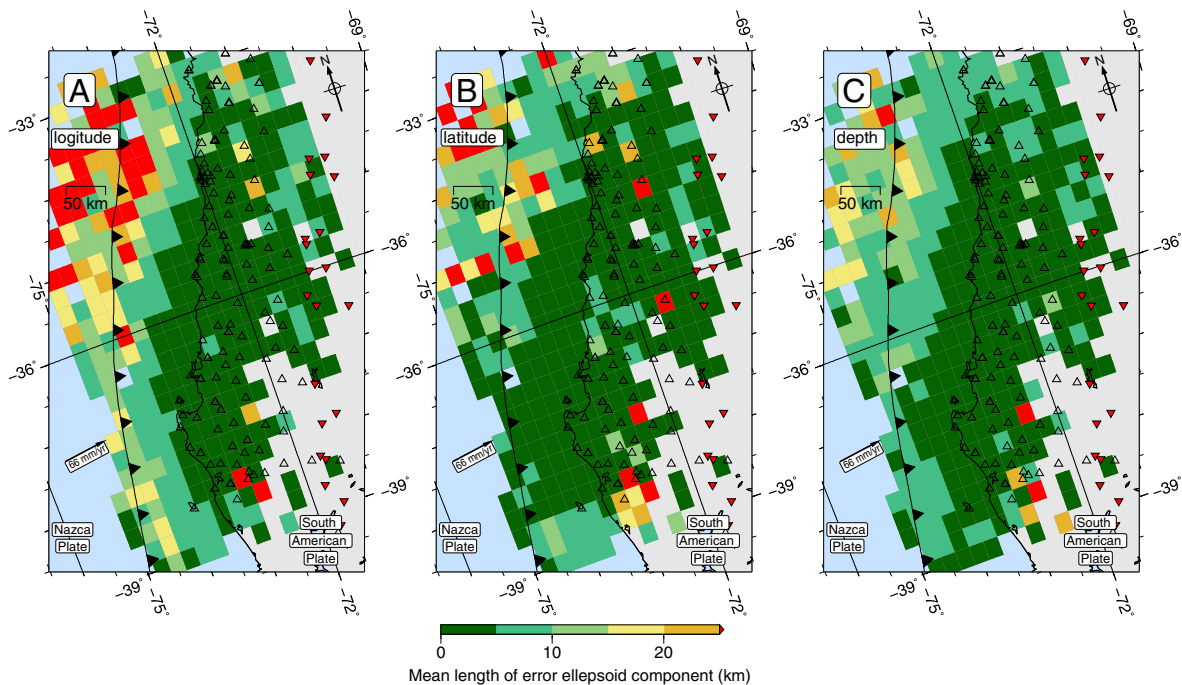
Fig. 6. Mean uncertainties based on error ellipsoids (68% confidence) from NonLinLoc for $0.25 \times 0.25°$ tiles for the events shown in Fig. 5. Depth errors for shallow events outside the network cannot grow as large as the horizontal errors because the oct-tree search algorithm can only explore the PDF within the pre-defined grid, which in this case ranges from 2 km above to 98 km below sea level. As a result the error ellipses of the depth errors cannot grow in two directions and start to saturate for shallow events with a small number of observations. This can be seen in the smaller mean length of the error ellipsoids for the events beneath the trench where the vertical component of the error ellipsoid is in average smaller than the mean lengths of the horizontal components. Volcanoes shown with red inverted triangles, stations with black triangles. A: Mean longitude uncertainty, B: latitude uncertainty, C: depth uncertainty.
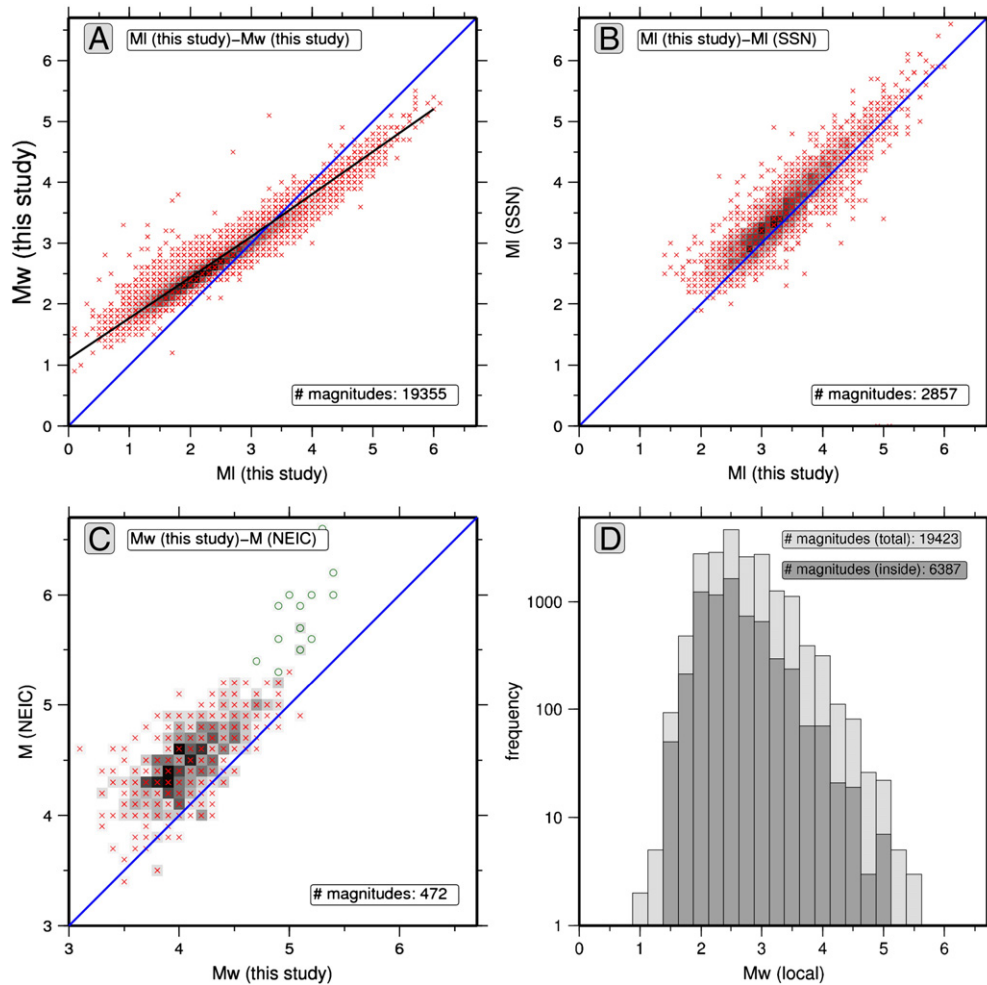
Fig. 7. Properties of the magnitudes estimated from the local network data. A: M_l versus M_w. The grey colours in the background indicate the amount of magnitude pairs. The black line has a slope of 2/3. B: M_l versus M_l from the SSN catalogue. C: M_w plotted versus magnitudes from the NEIC catalogue. M_b (M_w) from the NEIC catalogue is indicated with red crosses (green circles). D: Histogram of M_w for all events shown in light grey, events inside the network (GAP<180°) in dark grey.

5. Results and discussion

The local catalogue presented here reveals the detailed post-seismic seismicity along the complete rupture zone of the 27 February 2010 Maule earthquake. Fig. 5 shows the locations from the CMM detections and MPX picks merged with additional detections from Binder (Fig. S4) and events from the Chilean catalogue provided by the Servicio Sismológico Nacional de Chile (SSN) (Fig. S6) which were often not detected by CMM because they are far outside the network. Based on the spatial distribution of aftershocks (Fig. 5 and video S7) we identify six distinct groups of events along the rupture zone of the 2010 Maule earthquake which are discussed below. Additionally, we discuss a group of possible foreshocks visible in the global catalogues.

### 5.1. Normal faulting events beneath the outer rise

Near 35°S and in the southern part of the rupture at 38°S significant aftershock activity occurs beneath the outer rise such as the M_w 7.4 event (Fig. 2) which occurred 90 min after the mainshock. The CMT mechanisms indicate exclusively normal faulting events (Fig. 8). These extensional events with trench-parallel strikes are often observed for aftershocks beneath the outer rise after large subduction zone events because the outer rise is temporarily in tension due to the underthrusting motion of the oceanic plate (e.g., Christensen and Ruff, 1988). The

hypocentral depths of the events in this region are not well constrained because they occur far outside of our local network.

5.2. Seismicity associated with the seismogenic zone

Pronounced trench-parallel seismicity is apparent at 25–35 km depth and 50–120 km trench-perpendicular distance. In the central and southern parts of the 2010 Maule rupture it is visible as an inclined band of seismicity (Fig. 5, profiles B–D); this is less clear in the north as the band merges with intense crustal seismicity (Fig. 5, profile A). The majority of events within this group are offshore, which means that depths become progressively less reliable with increasing distance from the coast. Because the events offshore are located outside the network local focal mechanisms are not available. However, the vast majority of CMT solutions for events in this group are shallow thrusts (Fig. 8), indicating that these events are associated with the plate interface.

The along-strike extent of this group is similar to that of the coseismic rupture. Just as the northern coseismic slip patch has a much larger displacement than the southern one, more aftershocks in this group are found in the northern part of the rupture zone compared to the South. However, the aftershocks extend ~50 km further north than the coseismic slip as can be seen in the map view (Fig. 5). The plate interface seismicity also does not seem to be reduced in the
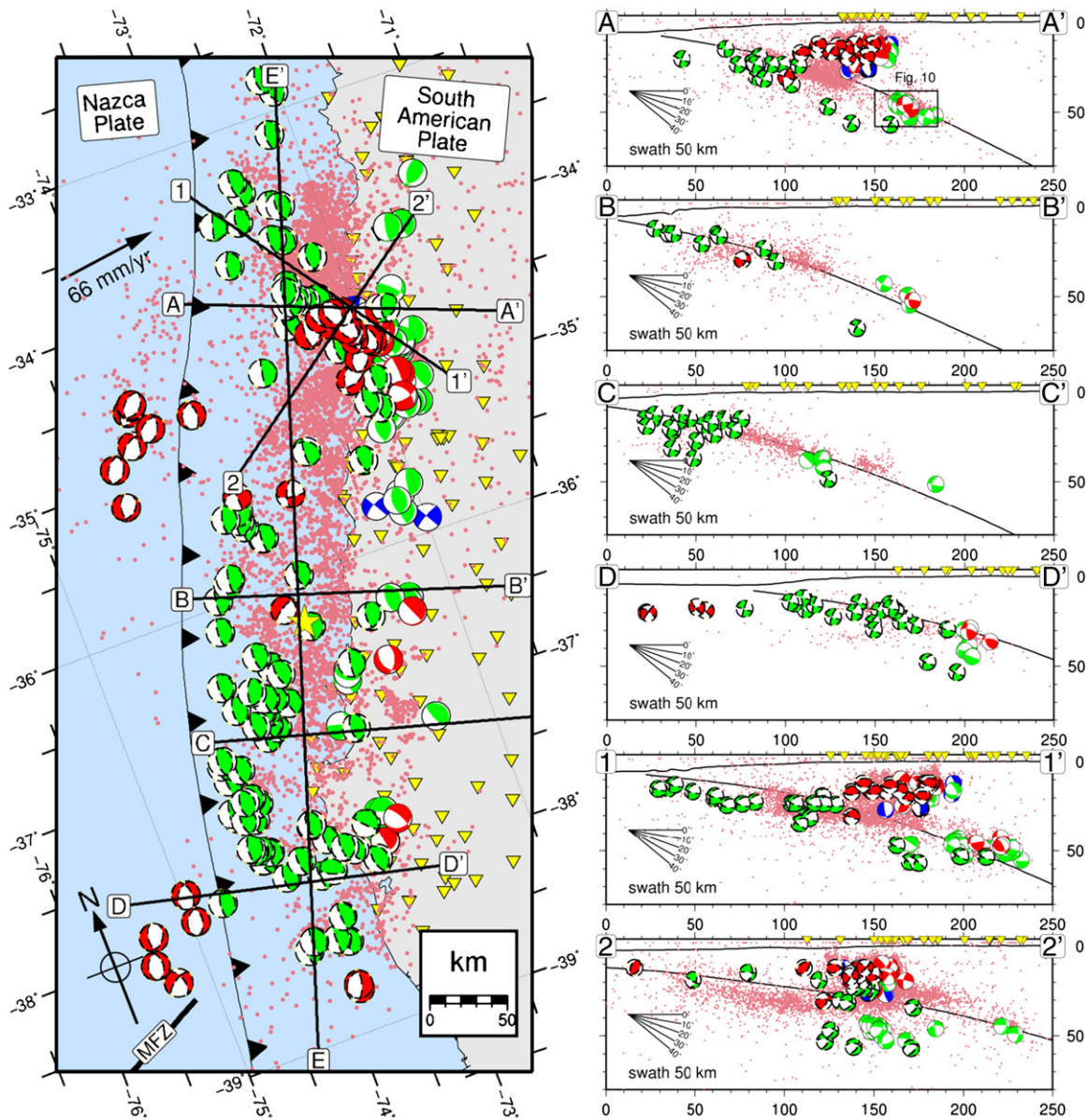
Fig. 8. Focal mechanisms from local data shown together with double-couple solutions from the global CMT catalogue (encircled with dashed line, $M_w \geq 5$, 27 February 2010–October 2010, double couple component only). Green focal mechanisms indicate thrust events, red represents normal faults and blue events show strike-slip faulting. Pink circles indicate hypocentres of events with more than 12 P arrivals. Left: Mapview. Focal mechanisms are shown as lower hemisphere projections. MFZ: Mocha Fracture Zone. Right panels: Trench parallel profiles (A–D) and profiles across the seismicity near Pichilemu (1 and 2). Focal mechanisms are shown as far hemisphere projections (lateral back projection onto vertical profile).

central minimum of the slip distribution near the epicentre. The fine structure of the seismicity shows various linear features oriented obliquely to the trench. Particularly prominent is a lineation in the south of the rupture area (near 73.5°W, 38°S) striking in WSW-direction sub-parallel to the Mocha fracture zone. Incoming plate structure influencing forearc seismicity has been observed in other subduction zones, e.g., where a major fracture zone, the Investigator Fracture Zone subducts below Sumatra (Lange et al., 2010). In both cases the trend of the incoming feature is approximately parallel to the convergence vector. Unfortunately, nearly all events within the lineation are offshore, making it difficult to unambiguously associate them with either the plate interface or the overriding or downgoing plate. Aftershocks and coseismic slip of the 2010 Maule earthquake terminate ~50 km south of the prolongation of the subducting Mocha Fracture zone (Fig. 5) around 38.5°S and overlap ~110 km with the 1960 earthquake region.

In the dip direction, the events are within the region of significant coseismic slip of the Lorito et al. (2011) slip model, but generally prefer the downdip side of the peak slip (see map view of Fig. 5 and compare the histogram and slip plot in profiles B and C). Only immediately to the west and northwest of the epicentre we find significant plate interface seismicity updip of the coseismic rupture (depths for this sub-group in the map view of Fig. 5 indicate depths too large for the plate interface but these are poorly constrained, and CMT focal mechanisms and depths (Fig. 8, profile B) support a plate interface origin for these events, too). A large number of plate interface aftershocks within the region which failed coseismically is unusual, as often a large number of aftershocks tend to avoid the area of large coseismic slip (Das and Henry, 2003; Perfettini et al., 2010; Tilmann et al., 2010). However, the location of slip in the up-dip direction offshore is the most poorly constrained feature of the slip models, which rely primarily on onshore geodetic

measurements. For example, if we compare the aftershock distribution with the coseismic slip model of Vigny et al. (2011), then a large portion of the plate interface seismicity is downdip of the region of significant coseismic slip (Fig. 9A).

The region between updip of this group and the trench is imaged as a wedge-shaped body by active seismic profiles (Moscoso et al., 2011). This ~40 km wide zone of reduced velocities, which is interpreted as a frontal accretionary prism consisting of unconsolidated sediments (Contreras-Reyes et al., 2010), is characterised by a significantly reduced number of aftershocks (Fig. 2) and lower moment release (Fig. 9B). The change from aseismic to seismic behaviour coincides spatially with the contact between the frontal accretionary prism and the paleo-accretionary prism (Moscoso et al., 2011). In contrast to the absence of larger events seen in the teleseismic catalogues a small number of local events occur in the zone where unconsolidated sediments are located, in particular north of 35°S.

5.3. Deep band of plate interface seismicity

A secondary deeper band of seismicity can be identified at 40–50 km depth and 130–180 km distance to the trench between 33.5°S and 37.5°S (Fig. 5, profiles A–C). In spite of some scatter, the events within this band describe a plane with a dip of ~28° (Fig. 10), close to the inferred slab dip in the SLAB1.0 reference model (Hayes and Wald, 2009). Most focal mechanisms based on first motion polarities show shallowly dipping thrust mechanisms with dips consistent with the overall dip of the cluster (Figs. 8 and 10), which indicates
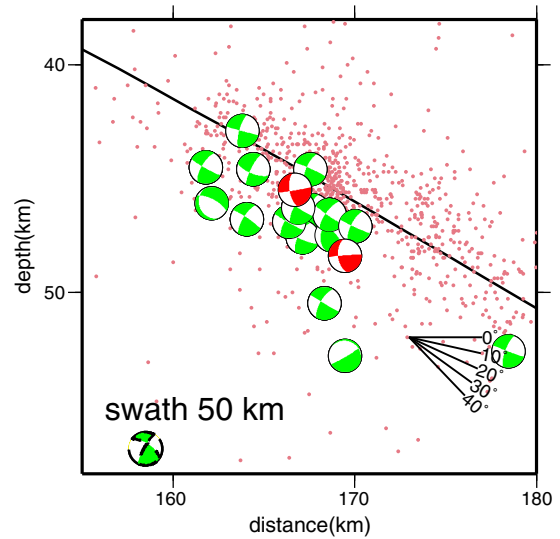

Fig. 10. Vertical profile showing a closeup of the focal mechanisms of the deep band, downdip of the coseismic slip. The location of the profile is indicated in Fig. 8, profile A. Colours of focal mechanisms (plotted as far hemisphere projections onto vertical profile) are the same as in Fig. 8.

that most of the events in this group rupture the plate interface. In map view, the band is not truly continuous but falls into several sub-clusters which are elongated parallel to the trench. It is notable, that
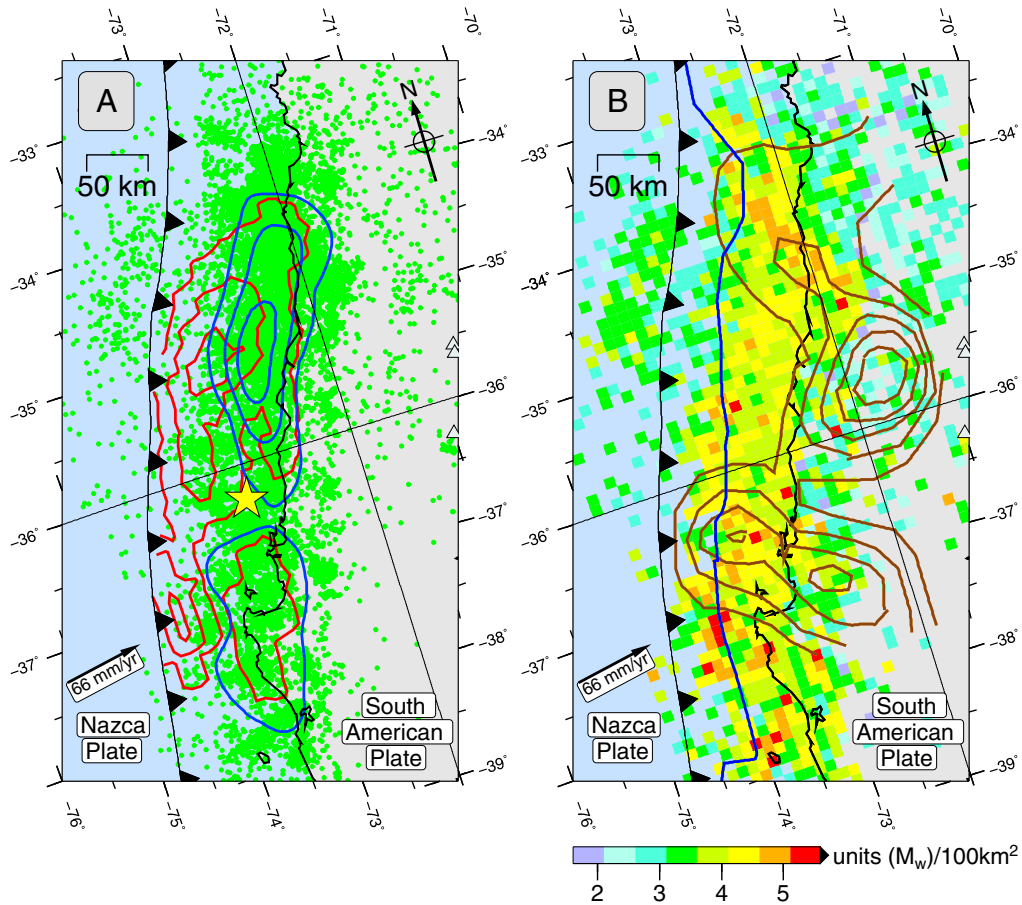

Fig. 9. Coseismic and postseismic slip models plotted together with the local aftershock seismicity and cumulative moment magnitude release. Left: Coseismic slip model (5 m slip contours) from Lorito et al. (2011) (based on geodetic and tsunami data) is shown in blue and the coseismic slip model from Vigny et al. (2011) (based on GPS data) in red. Local seismicity is shown with green circles. Right: The colour squares indicate the cumulative moment release estimated from the local seismicity, converted to equivalent moment magnitude. For the summation of the seismic moments we assumed that the moment is concentrated at the epicentre. The blue line indicates location of the eastern termination of the frontal accretionary prism (Contreras-Reyes et al., 2010). 12 day post-seismic afterslip (10 cm contours) from Vigny et al. (2011) is superimposed with brown lines.

the most active cluster within the deep band near 34.8°S, 71.8°W lines up with the intense NW–SE oriented crustal seismicity (Fig. 5, profile A, described below, Section 5.6). On a large scale, the deep interface seismicity levels correlate with the pattern of shallow plate interface activity (discussed above in Section 5.2) and coseismic slip, i.e., the northern part of the rupture zone is more active than the southern one. Similar to the shallower seismicity (Section 5.2), the deeper band extends in the north well beyond the coseismic rupture, and the slip minimum near the epicentre is not reflected in the after-shock frequency. Although the deep band lies along the continuation of the shallow one (Section 5.2), it is clearly separated from it by a 20–30 km wide gap with sparse or absent interface seismicity (Fig. 5, profiles A–C), and both its trenchward and landward ends are clearly demarcated.

Although there are other examples of megathrust aftershocks having clusters or bands of seismicity updip and downdip of the coseismic rupture (e.g., megathrust earthquakes in Sumatra in 2004, 2005 and 2007 had either one or both types of events (Collings et al., in press; Engdahl et al., 2007; Lange et al., 2010; Tilmann et al., 2010); similarly the M_w 7.8 Tocopilla earthquake of 2007 in Northern Chile (Motagh et al., 2010), the existence of two clearly distinguished groups of plate interface seismicity downdip of the coseismic rupture is rare; we are not aware of any other megathrust aftershock sequence showing similar behaviour.

These events occur within a depth range which showed minimal coseismic slip and the strongest afterslip as modelled by Vigny et al. (2011) (Fig. 9B), suggesting that the deep events might be driven by afterslip. However, similar to the coseismic slip, the afterslip patch does not extend as far north as the aftershocks in this group. Significant afterslip downdip of the coseismic rupture has been ob-served for other megathrust earthquakes (e.g. Hsu et al., 2006) with-out giving rise to two distinct bands. This raises the question what special conditions prevail along the Chilean margin which give rise to the deep band. A temperature of 350–450 °C is often thought (Hyndman et al., 1997) to mark a transition in frictional behaviour from unstable to stable based on the transition from velocity-weakening to velocity-strengthening in granite fault gouges (Blanpied et al., 1991). However, a recent thermal model (Völker et al., 2011) fitting heat flow measurements and other constraints at ~38°S shows a temperature of 350 °C to be reached only ~200 km beyond the deformation front at a depth of 72 km. As the incoming plate age increases (from 30 to 37 My, Müller et al., 1997) going northwards, and sediment cover is similar or less (Contreras-Reyes and Carrizo, 2011) we can conclude that the critical 350 °C temperature is only reached well beyond the deepest plate interface seismicity throughout the Maule segment.

Alternatively, the downdip transition in frictional properties has been related to the intersection of the plate interface with the continen-tal Moho below which serpentinisation of the mantle wedge is sup-posed to preclude unstable behaviour of the megathrust (Bostock et al., 2002; Hyndman et al., 1997); however, at least in a few regions, the seismogenic zone appears to extend below the mantle wedge (Dessa et al., 2009; Hino et al., 2000). Tong et al. (2010) stated that the downdip end of the coseismic rupture of the Maule event coincides approximately with the intersection point of plate interface and conti-nental Moho, but their Moho depth estimate was based on receiver function results from Northern Chile, which has a very different tectonic environment (e.g. erosive instead of accretionary margin), and on grav-ity models, which are inherently highly non-unique. Other studies of the structure of the Central Chilean margin which estimate the depth of the Moho based on gravity data (Tašárová, 2007; Tassara et al., 2006) or receiver functions (Yuan et al., 2006) suggest Moho depths of ~35 km. However, the resolution of the regions near the coast are low and further investigation is needed in order to better resolve the continental Moho depth, in particular for the northern part of the 2010 Maule rupture area. Currently, the best information about the

continental Moho is probably available for the southern part of the rup-ture zone from the tomographic model of Haberland et al. (2009) using data from a dense onshore/offshore network on and near the Arauco peninsula. In their model, the Moho deepens by nearly 20 km from its minimum below the Longitudinal Valley to the point of intersection with the plate interface, such that the intersec-tion is found nearly 200 km landward of the deformation front at a depth of ~50 km (orange lines in Fig. 5), more than 50 km land-ward of the position assumed by Tong et al. (2010). Below the magmatic arc Moho estimates based on receiver functions (Gilbert et al., 2006; Heit et al., 2008) indicate a Moho depth of ~50 km depth. This would place the southernmost extension of the deep seismic band wholly in the crust. As the one-dimensional model below the Arauco peninsula as determined by Haberland et al. (2009) is very similar to the one-dimensional model for the northern part of the rupture zone determined in this study (Fig. 4A), we consider it likely that the Moho intersec-tion occurs at a similar depth and distance to the trench through-out the rupture zone. If correct, this also implies that the downdip end of the coseismic rupture did not reach either the 350 °C or the Moho intersection. The uncertainty of the Haberland et al. tomographic model and its extrapolation to the north are such that we cannot determine with confidence whether the downdip end of the deep band coincides with the tip of the mantle wedge or whether the plate interface next to the lowermost conti-nental crust is aseismic. Haberland et al. (2009) also did not ob-serve the high v_p/v_s ratios which would be indicative of widespread hydration (serpentinisation) of the forearc mantle. In any case, as neither temperature nor the crust–mantle transition seems to be responsible for the onset of seismicity in the deep seis-mic band we must look at the crustal lithology.

The vast majority of seismicity within this group (Section 5.3) is locat-ed below the late Paleozoic batholith (green line, Fig. 5) (Martin et al., 1999). Adjacent west of the batholith, the "Eastern series", a low pres-sure/temperature unit of a paired metamorphic belt (Willner et al., 2009) is located. The seismic gap coincides spatially with this geologic boundary. The "Eastern series" and the late Paleozoic batholith are locat-ed all along the 2010 Maule rupture area which might indicate that the boundary between both is a deep-reaching feature. However, although there is a spatial relation between the geological structures of the ac-cretion complex and the Paleozoic batholith on the surface with the deep aftershock seismicity on the megathrust their genetic re-lation is unclear because the depth continuation of the geological units is not known, in particular the extent of the Paleozoic batho-lith to the west, beneath the Tertiary to recent sediments of the Longitudinal valley remains unclear.

An alternative possibility would be that the presence or thickness of the subduction channel controls the onset of seismicity. Reflectivity near the plate interface on a dense reflection profile at 38°S has been interpreted to be indicative of the presence of a subduction channel and is seen to a depth of ~35 km (Groß et al., 2008). This far south no clearly separated downdip group of seismicity is observed but the distribution of seismicity still shows two distinct peaks so that ar-guably the deeper band is still present but has moved up and sea-ward, merging with the shallower interplate seismicity (compare cross-sections Figs. 5C and D and accompanying histograms). If this interpretation is correct, then the up- and downdip limits of the shal-low plate interface band (Section 5.2) are controlled by sediment properties, and the downdip end of the deep group is controlled by the properties of lower crustal rocks. The updip limit of the deep band would then simply be the location where the subduction chan-nel pinches out. In most other subduction zones, the subduction channel might not reach as deep, such that the transition from sediment-controlled plate-interface to crustal rocks at the plate interface is not vis-ible in the seismicity, which would explain the absence of a deep plate in-terface band in most other megathrust aftershock sequences.

A further test of the viability of these or other ideas will require structural analysis, e.g. by tomography, beyond the scope of this seismicity study.

5.4. Sparse intermediate depth seismicity

Sparse intermediate depth seismicity originates from depths between 80 and 120 km (note that these events only show up in map view in Fig. 5). Before the 2010 Maule event most of the seismicity in Central Chile belonged to this cluster as can be seen from the EHB and SSN catalogues (Fig. 1 and Farías et al., 2010), and seismicity levels in this region actually do not appear to be significantly enhanced. It is likely that these intermediate depth events are intra-plate events within the subducted Nazca plate. Similar to the background seismicity, the intermediate depth aftershock seismicity becomes sparser to the south, which is related to the increasing temperature of the incoming plate (e.g., Kirby et al., 1996) from north to south due to a decrease of incoming plate age from 37 to 30 Ma (Müller et al., 1997) along the 2010 Maule rupture area. The intermediate depth seismicity occurs ~50 km west and parallel of the magmatic arc and the location of seismicity is similar before and after the 2010 rupture. Events within the downgoing plate downdip of the megathrust rupture have long been postulated to reflect downdip compression resulting from the large amount of slip on the shallow plate interface (Lay et al., 1989), similar to the way that normal-faulting events below the outer rise accommodate tensional stresses on the updip side of the rupture (Christensen and Ruff, 1988). However, the similarity of aftershock and background rates argues against a noticeable perturbation of the deeper slab by the Maule earthquake, in particular when set against the intense aftershock seismicity in the outer rise. The SSN catalogue lists 398 intermediate depth events ($M \geq 4$, latitudes between 34 and 39°S) for the time span 10 yr before the Maule 2010 earthquake and 43 events for the first year after the Maule earthquake.

5.5. Crustal events beneath the magmatic arc

Isolated shallow crustal seismicity up to magnitudes $M_l = 4.2$ occurred in the continental crust beneath the magmatic arc near Laguna del Dial (36.42°S, 71.1°W) and at 35°S. Both clusters are offset from Holocene volcanoes and were active before the earthquake. Comparing the event rates for events greater than $M_l = 4$ for the catalogue of the SSN for 1 yr after the Maule earthquake with 10 yr before suggests that the seismicity rate of crustal events along the magmatic arc is not strongly enhanced. However, activity within the crustal clusters along the magmatic arc is strongly enhanced in 2001 and 2005, which makes the rate comparison dependent on the exact time period chosen. From the time the local network is fully operational around 28 March 2010 we resolve crustal events beneath the Laguna del Dial indicating that stress transfer into the magmatic arc occurred in less than 1 month, if there is any. In total, 25 events with magnitudes between 1.7 and 3.9 were detected in these two clusters.

5.6. Crustal seismicity cluster near Pichilemu

A 145° oriented elongated cluster in map view (Figs. 2 and 5) hosted very pronounced aftershock activity near the city of Pichilemu. This cluster of seismicity occurs from the plate interface to the near surface and trends in the same direction as the strikes of the shallow strong aftershock doublet on 11 March 2010 near the city of Pichilemu. The first event ($M_w = 6.9$, 14:39:44 UTC) indicates normal faulting with 144° strike (Fig. 2) in the overriding plate. The mechanism of the second event ($M_w = 7.0$), 15 min later, strikes 159° and indicates a dip slip event, however this focal mechanism is presumably less trustworthy due to the close separation in time. On the same day another normal faulting event ($M_w = 5.6$, 20:11:27 UTC) occurred in the region indicating normal faulting with 146°

strike. These strike directions differ significantly from other major aftershocks ($M_w \geq 6.5$, Fig. 2) which have trench-parallel strikes. The orientation of the Pichilemu aftershock cluster is also similar to the mean direction of extensional surface cracks produced by the earthquake doublet on 11 March 2010 (Arriagada et al., 2011) but does not agree with the direction of previously known faults in the region such as the north–south trending left-lateral reverse Pichilemu–Vichuquén fault (e.g. Sernageomin, 2003; Willner et al., 2009). Therefore the observations indicate a previously unknown crustal structure with 145° strike extending ~75 km offshore. Based on the seismicity distribution of the high quality subset of local events (Fig. 5, dark red circles, profile 2–2′) we favour the SW dipping fault plane of the normal faulting events on 11 March 2010. Elsewhere along the southern Chilean margin NW–SE trending faults cutting through the forearc are well known, such as the Permian Lanalhue Fault Zone at 38° (Glodny et al., 2008).

In Northern Chile near the Mejillones Peninsula (23°S) normal faulting crustal faults are observed (e.g., Allmendinger and González, 2010), some of them just shortly after major megathrust events. Delouis et al. (1998) discuss possible mechanisms for the extensional faulting in the upper crust in great detail and present a model for extension in the upper crust assuming that coseismic deformation is more concentrated in the outer forearc than interseismic deformation. Delouis et al. (1998) suggest that the resulting net extension can accumulate over various seismic cycles and can produce normal faulting events in the overriding plate. The overall deviatoric extension in the shallow forearc is suggested to be reduced during the contractional, interseismic period. This reduction means that continental faults will remain locked and aseismic in the interseismic period of the subduction cycle (Delouis et al., 1998) and might explain the absence of significant shallow crustal seismicity during the interseismic period for the northern part of the 2010 Maule rupture (Fuenzalida et al., 1992; Pardo et al., 2002). Another factor which might favour the occurrence of the extensional cluster might be its location north-east of the coseismic slip maximum and might be a secondary effect related to large differential stress resulting from the large coseismic slip gradient there (Fig. 1). The recent work of Farías et al. (2011) shows that high Coulomb stress changes together with fluid flow as evidenced by high v_p/v_s values probably triggered the crustal faulting of the Pichilemu seismic cluster.

5.7. Small and moderate events on 21 January 2010

In the three months before the 27 February 2010 Maule earthquake only seven events are found in the wider study region (grey squares in Fig. 1) in the NEIC catalogue. Of these, three events (with magnitudes between 4.7 and 5.1) occurred on 21 January 2010 in the direct vicinity of the Maule mainshock hypocentre. These events as well as the epicentre itself are also located within a region, which was seismically active in the interseismic period, unlike most of the plate interface, which appeared to be fully locked and therefore devoid of seismic activity prior to the Maule rupture. Such a nucleation of a megathrust event within a region which is active during the interseismic period has been seen in previous great earthquakes, e.g. the Nias, Sumatra, earthquake in 2005 (Tilmann et al., 2010). Other great megathrust earthquakes also have been preceded by smaller events. For example, the M_w 9.0 Tohoku earthquake on 11 March 2011 was preceded by an M_w 7.2 event and its aftershocks two days before the mainshock; the 1960 Valdivia earthquake of May, 22 1960 was preceded by a series of fore-shocks up to M_w 8.1 that started on May, 21 (Cifuentes, 1989). However, the smaller magnitudes and much larger separation in time to the main shock of the January 21 events leave it ambiguous as to whether they should be considered foreshocks. Also, for other megathrust events no foreshock activity is seen in the epicentral area, e.g. the M_w 9.1 2004 earthquake in Northern Sumatra or the 1964 and 1965 events in Alaska.

6. Conclusion

The study of the automated hypocentre locations of aftershock of the M_w 8.8 earthquake on 27 February 2010 in Central Chile using a dense local aftershock network of landstations laterally covering the complete rupture zone reveals the structure and zones of postseismic aftershock stress release. The distribution of aftershocks shows a complex pattern where for the southern part of the rupture most of the events are related to the megathrust while in the northern part pronounced crustal seismicity is observed. Five trench parallel bands of seismicity are observed which are related to outer rise events, the seismogenic zone, afterslip downdip of the coseismic rupture associated with the plate interface, intermediate depth seismicity and the magmatic arc. Along the magmatic arc no significantly higher seismicity rate is observed for the first year after the mainshock. A pronounced cluster of crustal events near Pichilemu with mostly normal faulting and some strike-slip events occurs on an ~145° striking and SW-dipping structure and is suggested to release extensional strain which accumulated over several seismic cycles. In 50–120 km trench distance we find seismicity all along the 2010 Maule rupture area. Depending on the slip model considered this seismicity occurs in regions of high coseismic slip or downdip of the coseismic slip. A second seismic band at 40–50 km depth with thrust type events well aligned with the plate interface is best observed for the northern part of the 2010 Maule rupture zone north of 37°S below the Late Paleozoic batholith. Due to its location in regions of high postseismic activity and downdip of the coseismic rupture these events are suggested to be driven by afterslip. The lateral extent of the 2010 Maule aftershock seismicity and the coseismic slip distributions are clearly separated from incoming fracture zones such as the Juan Fernández Ridge in the North or the Mocha Fracture in the South. To the South the 2010 Maule earthquake might be limited by the slip pattern of the 1960 earthquake. For the northern termination of the 2010 rupture the aftershock seismicity extends beyond the coseismic slip by about ~50 km. The local catalogue can be requested by mail from the corresponding author.

Supplementary materials related to this article can be found online at http://dx.doi.org/10.1016/j.epsl.2011.11.034.

References

Aldersons, F., 2004. Toward three-dimensional crustal structure of the Dead Sea region from local earthquake tomography. Ph.D. thesis, Tel Aviv University, Israel.

Allmendinger, R.W., González, G., 2010. Neogene to Quaternary tectonics of the coastal Cordillera, northern Chile. Tectonophysics 495 (1–2), 93–110. doi:10.1016/j.tecto.2009.04.019.

Angermann, D., Klotz, J., Reigber, C., 1999. Space-geodetic estimation of the Nazca–South America Euler vector. Earth Planet. Sci. Lett. 171 (3), 329–334.

Arriagada, C., Arancibia, G., Cembrano, J., Martínez, F., Carrizo, D., Van Sint Jan, M., Sáez, E., González, G., Rebolledo, S., Sepúlveda, S., Contreras-Reyes, E., Jensen, E., Yañez, G., 2011. Nature and tectonic significance of co-seismic structures associated with the Mw 8.8 Maule earthquake, central southern Chile forearc. J. Struct. Geol. 33 (5), 891–897.

Barrientos, S.E., 1988. Slip distribution of the 1985 Central Chile earthquake. Tectonophysics 145 (3–4), 225–241. doi:10.1016/0040-1951(88)90197-7.

Barrientos, S.E., 1995. Dual seismogenic behavior: the 1985 Central Chile Earthquake. Geophys. Res. Lett. 22 (24), 3541–3544. doi:10.1029/95GL03316.

Bassin, C., Laske, G., Masters, G., 2000. The current limits of resolution for surface wave tomography in North America. EOS Trans. Am. Geophys. Union 81, F897.

Beck, S., Barrientos, S., Kausel, E., Reyes, M., 1998. Source characteristics of historic earthquakes along the central Chile subduction zone. J. S. Am. Earth Sci. 11 (2), 115–129. doi:10.1016/S0895-9811(98)00005-4.

Blanpied, M.L., Lockner, D.A., Byerlee, J.D., 1991. Fault stability inferred from granite sliding experiments at hydrothermal conditions. Geophys. Res. Lett. 18 (4), 609–612. doi:10.1029/91GL00469.

Bostock, M.G., Hyndman, R.D., Rondenay, S., Peacock, S.M., 2002. An inverted continental Moho and serpentinization of the forearc mantle. Nature 417 (6888), 536–538. doi:10.1038/417536a.

Campos, J., Hatzfeld, D., Madariaga, R., Lopez, G., Kausel, E., Zollo, A., Iannacone, G., Fromm, R., Barrientos, S., Lyon-Caen, H., 2002. A seismological study of the 1835 seismic gap in south-central Chile. Phys. Earth Planet. Inter. 132, 177–195.

Chlieh, M., Avouac, J.-P., Sieh, K., Natawidjaja, D.H., Galetzka, J., 2008. Heterogeneous coupling of the Sumatran megathrust constrained by geodetic and paleogeodetic measurements. J. Geophys. Res. 113 (B05305). doi:10.1029/2007JB004981.

Christensen, D.H., Ruff, L.J., 1988. Seismic coupling and outer rise earthquakes. J. Geophys. Res. 93 (B11), 13,421–13,444. doi:10.1029/JB093iB11p13421.

Cifuentes, I.L., 1989. The 1960 Chilean earthquakes. J. Geophys. Res. 94 (B1), 665–680.

Collings, R.E., Lange, D., Rietbrock, A., Tilmann, F., Natawidjaja, D.H., Suwargadi, B., Miller, M., Saul, J., (in press). Structure and seismogenic properties of the Mentawai segment of the Sumatra subduction zone revealed by local earthquake travel time tomography. J. Geophys. Res. doi:10.1029/2011JB008469.

Comte, D., Eisenberg, A., Lorca, E., Pardo, M., Ponce, L., Saragoni, R., Singh, S., Suarez, G., 1986. The 1985 Central Chile earthquake: a repeat of previous great earthquakes in the region? Science 233 (4762), 449–453. doi:10.1126/science.233.4762.449.

Contreras-Reyes, E., Carrizo, D., 2011. Control of high oceanic features and subduction channel on earthquake ruptures along the Chile–Peru subduction zone. Phys. Earth Planet. Inter. 186 (1–2), 49–58. doi:10.1016/j.pepi.2011.03.002.

Contreras-Reyes, E., Flueh, E.R., Grevemeyer, I., 2010. Tectonic control on sediment accretion and subduction off south central Chile: implications for coseismic rupture processes of the 1960 and 2010 megathrust earthquakes. Tectonics 29 (TC6018). doi:10.1029/2010TC002734 27 PP.

Darwin, C., 1840. XLII.—on the connection of certain volcanic phenomena in South America; and on the formation of mountain chains and volcanoes, as the effect of the same power by which continents are elevated. Transactions of the Geological Society of London, Series 2, 5, pp. 601–631. doi:10.1144/transgslb.5.3.601.

Das, S., Henry, C., 2003. Spatial relation between main earthquake slip and its aftershock distribution. Rev. Geophys. 41. doi:10.1029/2002RG000119.

Delouis, B., Philip, H., Dorbath, L., Cisternas, A., 1998. Recent crustal deformation in the Antofagasta region (northern Chile) and the subduction process. Geophys. J. Int. 132 (2), 302–338. http://dx.doi.org/10.1046/j.1365-246x.1998.00439.x.

Delouis, B., Nocquet, J., Vallée, M., 2010. Slip distribution of the February 27, 2010 Mw = 8.8 Maule earthquake, central Chile, from static and high-rate GPS, InSAR, and broadband teleseismic data. Geophys. Res. Lett. 37. doi:10.1029/2010GL043899.

Dessa, J., Klingelhoefer, F., Graindorge, D., André, C., Permana, H., Gutscher, M., Chauhan, A., Singh, S.C., SUMATRA-OBS Scientific Team, 2009. Megathrust earthquakes can nucleate in the forearc mantle: evidence from the 2004 Sumatra event. Geology 37 (7), 659–662. doi:10.1130/G25653A.1.

Di Stefano, R., Aldersons, F., Kissling, E., Baccheschi, P., Chiarabba, C., Giardini, D., 2006. Automatic seismic phase picking and consistent observation error assessment: application to the Italian seismicity. Geophys. J. Int. 165 (1), 121–134. doi:10.1111/j.1365-246X.2005.02799.x.

Diehl, T., Kissling, E., Husen, S., Aldersons, F., 2009. Consistent phase picking for regional tomography models: application to the greater Alpine region. Geophys. J. Int. 176 (2), 542–554. doi:10.1111/j.1365-246X.2008.03985.x.

Drew, J., Leslie, D., Armstrong, P., Michaud, G., 2005. Automated microseismic event detection and location by continuous spatial mapping. SPE Annual Technical Conference and Exhibition, 9–12 October 2005, Dallas, Texas. SPE 95513-PP.

Engdahl, E.R., Villasenor, A., DeShon, H.R., Thurber, C.F., 2007. Teleseismic relocation and assessment of seismicity (1918–2005) in the region of the 2004 Mw 9.0 Sumatra–Andaman and 2005 Mw 8.6 Nias Island great earthquakes. Bull. Seismol. Soc. Am. 97 (1), S43–S61. doi:10.1785/0120050614.

Farías, M., Comte, D., Charrier, R., Martinod, J., David, C., Tassara, A., Tapia, F., Fock, A., 2010. Crustal–scale structural architecture in central Chile based on seismicity and surface geology: implications for Andean mountain building. Tectonics 29 (TC3006). doi:10.1029/2009TC002480 22 PP.

Farías, M., Comte, D., Roecker, S., Carrizo, D., Pardo, M., 2011. Crustal extensional faulting triggered by the 2010 Chilean earthquake: the Pichilemu seismic sequence. Tectonics 30 (TC6010). doi:10.1029/2011TC002888 11 PP.

Fuenzalida, A., Pardo, M., Cisternas, A., Dorbath, L., Dorbath, C., Comte, D., Kausel, E., 1992. On the geometry of the Nazca Plate subducted under Central Chile (32–34.5°S) as inferred from microseismic data. Tectonophysics 205, 1–11. doi:10.1016/0040-1951(92)90413-Z.

Gilbert, H., Beck, S., Zandt, G., 2006. Lithospheric and upper mantle structure of central Chile and Argentina. Geophys. J. Int. 165 (1), 383–398. doi:10.1111/j.1365-246X.2006.02867.x.

Glodny, J., Echtler, H., Collao, S., Ardiles, M., Burón, P., Figueroa, O., 2008. Differential Late Paleozoic active margin evolution in South-Central Chile (37°S–40°S)—the Lanalhue Fault Zone. J. S. Am. Earth Sci. 26 (4), 397–411. doi:10.1016/j.jsames.2008.06.001.

Groß, K., Micksch, U., TIPTEQ Research Group, Seismics Team, 2008. The reflection seismic survey of project TIPTEQ—the inventory of the Chilean subduction zone at 38.2°S. Geophys. J. Int. 172 (2), 565–571. doi:10.1111/j.1365-246X.2007.03680.x.

Haberland, C., Rietbrock, A., Lange, D., Bataille, K., Hofmann, S., 2006. Interaction between forearc and oceanic plate at the south-central Chilean margin as seen in local seismic data. Geophys. Res. Lett. 33, L233023. doi:10.1029/2006GL028189.

Haberland, C., Rietbrock, A., Lange, D., Bataille, K., Dahm, T., 2009. Structure of the seismogenic zone of the southcentral Chilean margin revealed by local earthquake travel-time tomography. J. Geophys. Res. 114, B01317. doi:10.1029/2008JB005802.

Hanks, T.C., Boore, D.M., 1984. Moment–magnitude relations in theory and practice. J. Geophys. Res. 89 (B7), 6229–6235. doi:10.1029/JB089iB07p06229.

Hayes, G.P., Wald, D.J., 2009. Developing framework to constrain the geometry of the seismic rupture plane on subduction interfaces a priori—a probabilistic approach. J. Geophys. Res. 176 (3), 951–964. doi:10.1111/j.1365-246X.2008.04035.x.

Heit, B., Yuan, X., Bianchi, M., Sodoudi, F., Kind, R., 2008. Crustal thickness estimation beneath the southern central Andes at 30°S and 36°S from S wave receiver function analysis. Geophys. J. Int. 174 (1), 249–254. doi:10.1111/j.1365-246X.2008.03780.x.

Hino, R., Ito, S., Shiobara, H., Shimamura, H., Sato, T., Kanazawa, T., Kasahara, J., Hasegawa, A., 2000. Aftershock distribution of the 1994 Sanriku-oki earthquake (Mw 7.7) revealed by ocean bottom seismographic observation. J. Geophys. Res. 105 (B9), 21,697–21,710. doi:10.1029/2000JB900174.

Hsu, Y.-J., Simons, M., Avouac, J.-P., Galetzka, J., Sieh, K., Chlieh, M., Natawidjaja, D., Prawirodirdjo, L., Bock, Y., 2006. Frictional afterslip following the 2005 Nias–Simeulue earthquake, Sumatra. Science 312 (5782), 1921–1926. doi:10.1126/science.1126960.

Hutton, L.K., Boore, D.M., 1987. The ML scale in Southern California. Bull. Seismol. Soc. Am. 77 (6), 2074–2094.

Hyndman, R.D., Yamano, M., Oleskevich, D.A., 1997. The seismogenic zone of subduction thrust faults. Island Arc 6 (3), 244–260. doi:10.1111/j.1440-1738.1997.tb00175.x.

Kirby, S., Engdahl, E.R., Denlinger, R., 1996. Intermediate-depth intraslab earthquakes and arc volcanism as physical expressions of crustal and uppermost mantle metamorphism in subducting slabs. In: Bebout, E., Scholl, W., Kirby, H., Platt, P. (Eds.), Subduction Top to Bottom. : Geophysical Monograph Series. American. Geophysical Union, Washington D.C, pp. 195–214.

Kissling, E., Ellsworth, W.L., Eberhart-Phillips, D., Kradolfer, U., 1994. Initial reference models in local earthquake tomography. J. Geophys. Res. 99 (B10), 19.635–19.646.

Konca, A.O., Avouac, J.-P., Sladen, A., Meltzner, A.J., Sieh, K., Fang, P., Li, Z., Galetzka, J., Genrich, J., Chlieh, M., Natawidjaja, D.H., Bock, Y., Fielding, E.J., Ji, C., Helmberger, D.V., 2008. Partial rupture of a locked patch of the Sumatra megathrust during the 2007 earthquake sequence. Nature 456, 631–635.

Lange, D., Cembrano, J., Rietbrock, A., Haberland, C., Dahm, T., Bataille, K., 2008. First seismic record for intra-arc strike-slip tectonics along the Liquiñe-Ofqui fault zone at the obliquely convergent platemargin of the southern Andes. Tectonophysics 455 (1–4), 14–24. doi:10.1016/j.tecto.2008.04.014.

Lange, D., Tilmann, F., Rietbrock, A., Collings, R., Natawidjaja, D.H., Suwargadi, B.W., Barton, P., Henstock, T., Ryberg, T., 2010. The fine structure of the subducted investigator fracture zone in western Sumatra as seen by local seismicity. Earth Planet. Sci. Lett. 298 (1–2). doi:10.1016/j.epsl.2010.07.020.

Lay, T., Astiz, L., Kanamori, H., Christensen, D.H., 1989. Temporal variation of large intraplate earthquakes in coupled subduction zones. Phys. Earth Planet. Inter. 54 (3–4), 258–312. doi:10.1016/0031-9201(89)90247-1.

Lay, T., Ammon, C.J., Kanamori, H., Koper, K.D., Sufri, O., Hutko, A.R., 2010. Teleseismic inversion for rupture process of the 27 February 2010 Chile (M_w8.8) earthquake. Geophys. Res. Lett. 37. doi:10.1029/2010GL043379.

Lienert, B.R., Havskov, J., 1995. A computer program for locating earthquakes both locally and globally. Seismol. Res. Lett. 66 (5), 26–36. doi:10.1785/gssrl.66.5.26.

Lomax, A., Virieux, J., Volant, P., Berge, C., 2000. Probabilistic earthquake location in 3D and layered models: introduction of a Metropolis–Gibbs method and comparison with linear locations. In: Thurber, C., Rabinowitz, N. (Eds.), Advances in Seismic Event Location. Kluwer, Amsterdam, pp. 101–134.

Lorito, S., Romano, F., Atzori, S., Tong, X., Avallone, A., McCloskey, J., Cocco, M., Boschi, E., Piatanesi, A., 2011. Limited overlap between the seismic gap and coseismic slip of the great 2010 Chile earthquake. Nat. Geosci. 4 (3), 173–177. doi:10.1038/ngeo1073.

Martin, M.W., Kato, T.T., Rodriguez, C., Godoy, E., Duhart, P., McDonough, M., Campos, A., 1999. Evolution of the late Paleozoic accretionary complex and overlying forearc–magmatic arc, south central Chile (38°–41°S): constraints for the tectonic setting along the southwestern margin of Gondwana. Tectonics 18 (4), 582–605. doi:10.1029/1999TC900021.

McCann, W.R., Nishenko, S.P., Sykes, L.R., Krause, J., 1979. Seismic gaps and plate tectonics: seismic potential for major boundaries. Pure Appl. Geophys. 117 (6), 1082–1147. doi:10.1007/BF00876211.

Mendoza, C., Hartzell, S., 1988. Aftershock patterns and main shock faulting. Bull. Seismol. Soc. Am. 78 (4), 1438–1449.

Moreno, M.S., Bolte, J., Klotz, J., Melnick, D., 2009. Impact of megathrust geometry on inversion of coseismic slip from geodetic data: application to the 1960 Chile earthquake. Geophys. Res. Lett. L16310 (36). doi:10.1029/2009GL039276.

Moreno, M., Melnick, D., Rosenau, M., Bolte, J., Klotz, J., Echtler, H., Baez, J., Bataille, K., Chen, J., Bevis, M., Hase, H., Oncken, O., 2011. Heterogeneous plate locking in the South-Central Chile subduction zone: building up the next great earthquake. Earth Planet. Sci. Lett. 305 (3–4), 413–424. doi:10.1016/j.epsl.2011.03.025.

Moscoso, E., Grevemeyer, I., Contreras-Reyes, E., Flueh, E.R., Dzierma, Y., Rabbel, W., Thorwart, M., 2011. Revealing the deep structure and rupture plane of the 2010 Maule, Chile earthquake (Mw = 8.8) using wide angle seismic data. Earth Planet. Sci. Lett. 307 (1–2), 147–155. doi:10.1016/j.epsl.2011.04.025.

Motagh, M., Schurr, B., Anderssohn, J., Cailleau, B., Walter, T.R., Wang, R., Villotte, J.-P., 2010. Subduction earthquake deformation associated with 14 November 2007, Mw 7.8 Tocopilla earthquake in Chile; results from InSAR and aftershocks. Tectonophysics 490 (1–2), 60–68. doi:10.1016/j.tecto.2010.04.033.

Müller, R.D., Roest, W.R., Royer, J.-Y., Gahagan, L.M., Sclater, J.G., 1997. Digital isochrons of the world's ocean floor. J. Geophys. Res. 102 (B2), 3211–3214.

Nippress, S.E.J., Rietbrock, A., Heath, A.E., 2010. Optimized automatic pickers: application to the ANCORP data set. Geophys. J. Int.. doi:10.1111/j.1365-246X.2010.04531.x

Oleskevich, D.A., Hyndman, R.D., Wang, K., 1999. The updip and downdip limits to great subduction earthquakes: thermal and structural models of Cascadia, south Alaska, SWJapan, and Chile. J. Geophys. Res. 104 (B7), 14.965–14.991.

Ottemöller, L., Havskov, J., 2003. Moment magnitude determination for local and regional earthquakes based on source spectra. Bull. Seismol. Soc. Am. 93 (1), 203–214. doi:10.1785/0120010220.

Pardo, M., Comte, D., Monfret, T., 2002. Seismotectonic and stress distribution in the central Chile subduction zone. J. S. Am. Earth Sci. 15 (1), 11–22. doi:10.1016/S0895-9811(02)00003-2.

Perfettini, H., Avouac, J.P., Tavera, H., Kositsky, A., Nocquet, J.M., Bondoux, F., Chlieh, M., Sladen, A., Audin, L., Farber, D.L., Soler, P., 2010. Seismic and aseismic slip on the Central Peru megathrust. Nature 465 (7294), 78–81.

Plafker, G., Savage, J.C., 1970. Mechanism of the Chilean earthquakes of May 21 and 22, 1960. Geol. Soc. Am. Bull. 81 (4), 1.001–1.030.

Podvin, P., Lecomte, L., 1991. Finite difference computation of traveltimes in very contrasted velocity models: a massively parallel approach and its associated tools. Geophys. J. Int. 105, 271–284. doi:10.1111/j.1365-246X.1991.tb03461.x.

Pollitz, F.F., Brooks, B., Tong, X., Bevis, M.G., Foster, J.H., Bürgmann, R., Smalley, R.J., Vigny, C., Socquet, A., Ruegg, J.-C., Campos, J., Barrientos, S., Parra, H., Baez Soto, J.-C., Cimbaro, S., Blanco, M., 2011. Coseismic slip distribution of the February 27, 2010 Mw 8.8 Maule, Chile earthquake. Geophys. Res. Lett. 38 (L09309). doi:10.1029/2011GL047065.

Reasenberg, P.A., Oppenheimer, D., 1985. FPFIT, FPPLOT, and FPPAGE: Fortran computer programs for calculating and displaying earthquake fault-plane solutions. Open-File Rep. 85–739, U.S. Geol. Surv.

Ruegg, J., Rudloff, A., Vigny, C., Madariaga, R., de Chabalier, J.B., Campos, J., Kausel, E., Barrientos, S., Dimitrov, D., 2009. Interseismic strain accumulation measured by GPS in the seismic gap between Constitución and Concepción in Chile. Phys. Earth Planet. Inter. 175 (1–2), 78–85. doi:10.1016/j.pepi.2008.02.015.

Sernageomin, 2003. Mapa Geológico de Chile: versión digital, N°4, CD-ROM, versión 1.0. Servicio Nacional de Geología y Minería. Servicio Nacional de Geología y Minería, Publicación Geológica Digital, Santiago, Chile.

Tašárová, Z.A., 2007. Towards understanding the lithospheric structure of the southern Chilean subduction zone (36°S–42°S) and its role in the gravity field. Geophys. J. Int. 170 (3), 995–1014. doi:10.1111/j.1365-246X.2007.03466.x.

Tassara, A., Götze, H.-J., Schmidt, S., Hackney, R., 2006. Three-dimensional density model of the Nazca plate and the Andean continental margin. J. Geophys. Res. 111 (B09404). doi:10.1029/2005JB003976.

Tilmann, F.J., Craig, T.J., Grevemeyer, I., Suwargadi, B., Kopp, H., Flueh, E., 2010. The updip seismic/aseismic transition of the Sumatra megathrust illuminated by aftershocks of the 2004 Aceh–Andaman and 2005 Nias events. Geophys. J. Int. 181 (3), 1261–1274. doi:10.1111/j.1365-246X.2010.04597.x.

Tong, X., Sandwell, D., Luttrell, K., Brooks, B., Bevis, M., Shimada, M., Foster, J., Smalley Jr., R., Parra, H., Soto, J.C.B., Blanco, M., Kendrick, E., Genrich, J., Caccamise II, D.J., 2010. The 2010 Maule, Chile earthquake: downdip rupture limit revealed by space geodesy. Geophys. Res. Lett. 37. doi:10.1029/2010GL045805.

Vigny, C., Socquet, A., Peyrat, S., Ruegg, J.-C., Métois, M., Madariaga, R., Morvan, S., Lancieri, M., Lacassin, R., Campos, J., Carrizo, D., Bejar-Pizarro, M., Barrientos, S., Armijo, R., Aranda, C., Valderas-Bermejo, M.-C., Ortega, I., Bondoux, F., Baize, S., Lyon-Caen, H., Pavez, A., Vilotte, J.P., Bevis, M., Brooks, B., Smalley, R., Parra, H., Baez, J.-C., Blanco, M., Cimbaro, S., Kendrick, E., 2011. The 2010 Mw 8.8 Maule megathrust earthquake of Central Chile, monitored by GPS. Science 332 (6036), 1417–1421. doi:10.1126/science.1204132.

Völker, D., Grevemeyer, I., Stipp, M., Wang, K., He, J., 2011. Thermal control of the seismogenic zone of southern Central Chile. J. Geophys. Res. doi:10.1029/2011JB008247.

Wessel, P., Smith, W.H.F., 1998. New, improved version of the Generic Mapping Tools released. suppl. to EOS. Transactions, AGU, 79, p. 579.

Willner, A., Richter, P., Ring, U., 2009. Structural overprint of a late Paleozoic accretionary system in north-central Chile (34–35°S) during post-accretional deformation. Andean Geol. 36, 17–36.

Yáñez, G.A., Ranero, C.R., von Huene, R., Díaz, J., 2001. Magnetic anomaly interpretation across the southern central Andes (32°S–34°S): the role of the Juan Fernandez Ridge in the late Tertiary evolution of the margin. J. Geophys. Res. 106 (B4), 6.325–6.345.

Yuan, X., Asch, G., Bataille, K., Bock, G., Bohm, M., Echtler, H., Kind, R., Oncken, O., Wölbern, I., 2006. Deep seismic images of the Southern Andes. In: Kay, S.M., Ramos, V.A. (Eds.), Evolution of an Andean Margin: A Tectonic and Magmatic View from the Andes to the Neuquén Basin (35°–39°S lat): Geol. Soc. Am. Special Paper 407. Geol. Soc. Am. , pp. 61–72. doi:10.1130/2006.2407(03).